OPEN ACCESS
IOP Publishing | IMMT
International Journal of Extreme Manufacturing
Int. J. Extrem. Manuf. **6** (2024) 045004 (14pp)
https://doi.org/10.1088/2631-7990/ad3c7f

Polar-coordinate line-projection light-curing continuous 3D printing for tubular structures

Huiyuan Wang[1,5], Siqin Liu[2,5], Xincheng Yin[1,5], Mingming Huang[3], Yanzhe Fu[1], Xun Chen[1], Chao Wang[1], Jingyong Sun[4], Xin Yan[2,*], Jianmin Han[3,*], Jiping Yang[4], Zhijian Wang[4,*], Lizhen Wang[1], Yubo Fan[1,*] and Jiebo Li[1,*]

[1] Key Laboratory of Biomechanics and Mechanobiology (Beihang University), Ministry of Education, Institute of Medical Photonics, Beijing Advanced Innovation Center for Biomedical Engineering, School of Biological Science and Medical Engineering, Beihang University, Beijing 100191, People's Republic of China
[2] School of Mechanical Engineering and Automation, Beihang University, Beijing 100191, People's Republic of China
[3] Peking University School and Hospital of Stomatology, Beijing 100081, People's Republic of China
[4] School of Materials Science and Engineering, Beihang University, Beijing 100191, People's Republic of China

E-mail: yan_xin@buaa.edu.cn, hanjianmin@bjmu.edu.cn, zhijianw@buaa.edu.cn, yubofan@buaa.edu.cn and jiebo39@buaa.edu.cn

Received 18 December 2023, revised 15 January 2024
Accepted for publication 9 April 2024
Published 23 April 2024

Abstract

3D printing techniques offer an effective method in fabricating complex radially multi-material structures. However, it is challenging for complex and delicate radially multi-material model geometries without supporting structures, such as tissue vessels and tubular graft, among others. In this work, we tackle these challenges by developing a polar digital light processing technique which uses a rod as the printing platform. The 3D model fabrication is accomplished through line projection. The rotation and translation of the rod are synchronized to project and illuminate the photosensitive material volume. By controlling the distance between the rod and the printing window, we achieved the printing of tubular structures with a minimum wall thickness as thin as 50 micrometers. By controlling the width of fine slits at the printing window, we achieved the printing of structures with a minimum feature size of 10 micrometers. Our process accomplished the fabrication of thin-walled tubular graft structure with a thickness of only 100 micrometers and lengths of several centimeters within a timeframe of just 100 s. Additionally, it enables the printing of axial multi-material structures, thereby achieving adjustable mechanical strength. This method is conducive to rapid customization of tubular grafts and the manufacturing of tubular components in fields such as dentistry, aerospace, and more.

[5] These authors contributed equally to this work.
[*] Authors to whom any correspondence should be addressed.

2631-7990/24/045004+14$33.00

Supplementary material for this article is available online

Keywords: 3D printing, polar coordinate, line projection, light-curing, tubular structure, radially multi-material structures

1. Introduction

Tubular structures are common in nature, ranging from plant stems to animal blood vessels, and extending to the fuel tanks of rockets. This ubiquitous structural form finds widespread applications in diverse fields such as life sciences, medicine, and aerospace [1–5]. The manufacturing of tubular structures encompasses various methods, with many approaches available for producing smooth and seamless tubes. For instance, steel tubes can be manufactured through processes such as extrusion, drawing, and welding. However, specific types of tubular structures, such as tubular grafts, are typically fabricated using laser subtractive manufacturing [6–8]. The movement of the laser point allows the creation of various patterns on polymeric tubes. Nevertheless, achieving tubular grafts with fine features poses significant challenges during the manufacturing process, as polymer materials may undergo melting and mechanical stress, resulting in shape alterations. The production of multi-material tubular structures, like blood vessels with varying diameters along their length, is even more challenging, often requiring sophisticated microfluidic techniques. The thin-walled nature of vascular structures, with wall thickness significantly smaller than their length, further increases the complexity of manufacturing [9, 10].

Three-dimensional (3D) printing is a highly efficient fabrication technology, to fabricate the objects layer-by-layer with the computer aided design [11–13]. Many advanced 3D printing techniques, with fast printing speed and high precision have been developed in the past several decades, including fused deposition modeling (FDM) [14–16], continuous liquid interface production (CLIP) [17, 18], high-area rapid printing (HARP) [19], rapid continuous stereolithography based on volumetric polymerization inhibition patterning [20], dual-color xolography volumetric 3D printing [21, 22], volume 3D printing based on tomographic reconstruction [23–26], etc. The development of 3D printing technology has provided numerous advantages for manufacturing prototypes of tubular structures such as tubular grafts and biomimetic blood vessels [1, 27–30]. For example, van Lith *et al* used CLIP to achieve high-precision tubular graft of 2 cm long printing in less than 20 min [31]. Ware *et al* then used the same technique to increase the speed to 11.3 min [32]. In order to achieve different mechanical properties for the printing of multi-material scaffolds, Jia *et al* used FDM printed self-expandable tubular graft [33]. The desired shape is created by printing each layer in x–y plane and stacking different layers in z direction. Nevertheless, the tubular grafts usually have a large aspect ratio, with tiny tube diameter and long length, making it difficult to stand on the supporting plate stably. To address this problem, researchers have employed the rotating mandrel as the substrate, and used extrusion method to print the filaments onside [34–38]. The inner diameter of the printed vascular shape is determined by the size of rotating mandrel, and the resolution of rotating mandrel-assisted extrusion approach is typically around 0.1 mm, greatly limiting their applications in the microscale blood vessels. The development of a high-precision printing method for tubular materials is highly necessary.

The digital light processing (DLP) method is a projection technique, and has many advantages for 3D printing, such as fast printing speed, high surface quality, and intricate details. To fabricate a tubular graft, the substrate is immersed in the light curable reservoir and each layer which is obtained by slicing the tubular graft in z direction is cured with a patterned light illumination [39–42]. The DLP technique faces several challenges in printing tubular grafts. First, the printed object may have a problem in precision accuracy when the length is pretty long. Furthermore, when printing radially multi-material tubular structures, it is necessary to switch the photocurable resin in each layer, which is time-consuming and incurs higher costs. Therefore, it is desirable to develop a rapid and high-precision printing method that can address multi-material, polar-coordinate printing.

In this work, we develop a DLP printing setup with a rotating mandrel as the substrate, called Polar-coordinate Line-projection Light-curing Production (PLLP) technology. The patterned light illumination creates tiny solidified polymeric structures on the rotating mandrel. This is a printing method based on a polar coordinate system. PLLP offers several advantages in printing the tubular grafts. First, compared to the rotating extrusion printing method, the PLLP printing setup shows fast printing speed and higher printing resolution. Second, the integration of rotating mandrel offers great advantages in the printing radially multi-material structures. We first establish the slicing algorithm for this new setup, denoted as the polar line slicing (PLS) algorithm. A resin switching system is further developed in the PLLP setup to print hybrid radially multi-material tubular structures. Furthermore, PLLP has the capability to produce 3D structures beyond tubular configurations with the axis serving as the central point.

2. PLLP printing setup, parameters, and slicing method

Figure 1(a) illustrates the PLLP printing setup. A patterned light generated by DLP passes through a slit with a width of w and creates an illumination pattern on the photocurable resin. A rotatable mandrel is inserted in the transparent reservoir which is filled with photocurable resin. The resin would

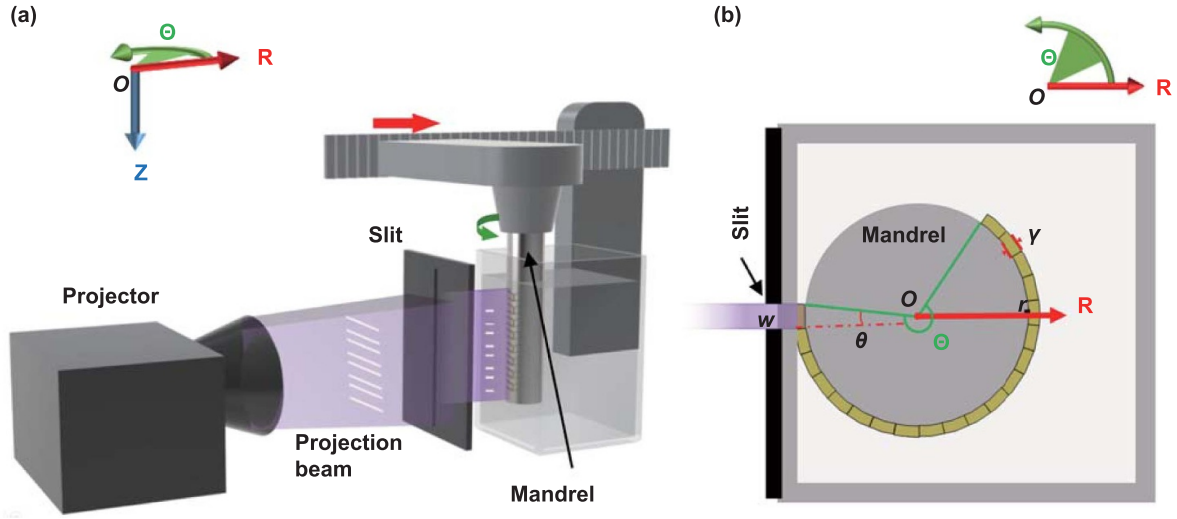

Figure 1. Schematic of a PLLP system. (a) PLLP setup schematic. (b) Top view of the printing process.

solidify under the illumination of the light, creating tiny voxel. As shown in the top view of the printing process, the width and thickness of the voxel depend on the slit width and the distance between the edge of reservoir and mandrel (figure 1(b)). After the solidification of the voxel, the mandrel would rotate with an angle of theta, and the light pattern could be changed accordingly. After the mandrel rotates for 360 degree, the light would create one layer of vascular structure with desired patterns. After that, the mandrel could move in R direction, driven by a line motor. The cured part would separate from the edge and uncured resin would replenish the part, which could repeat the photo printing process in the second layer. As a consequence of the rotational movement of the build platform after each layer, the cured components are displaced from the projection area, creating space for the introduction of fresh resin to replenish the original position. This mechanism facilitates the achievement of continuous printing.

2.1. Printing parameters of photocurable resins

To verify the performance of PLLP in the vascular structure, we screen the printing parameters, including the illumination time, thickness resolution, resolution in θ direction. These parameters are determined by the hardware of the PLLP device and the characteristics of the photocurable resin. The photoinitiator absorbs UV-light energy, generating free radicals to initiate the resin curing process. To achieve solidification, energy absorption greater than the curing threshold is required. However, excessive energy absorption can affect curing precision due to optical penetration depth and edge diffusion. The optical power of the projection device remains constant as 16.4 mW cm^{-2}. Resin experiences a change in refractive index during its curing process. This process can be monitored by a camera oriented perpendicular to the projection direction (movie 1). By analyzing the curing process, the correlation between the solidification thickness in the radial (R) direction and the projection time of the PLLP can be determined. In addition, the reactive thickness of the solidified portion must surpass the width between the mandrel and the walls of the reaction window. For instance, with a projection time of 500 millisecond, the actual reactive thickness measures 60 μm. However, the width γ between the mandrel and the walls of the reaction window needs to be less than 60 μm and also avoids the incompletely solidified section at the front end of the reaction. The final selected value for γ is 50 μm. Once the reaction time exceeds 1 s, the width of the unreacted portion starts to increase (figure S1), which is unfavorable for having disconnected structures in the intermediate layers during printing. For a reaction time of 1 s, the layer thickness γ is set to 100 μm. Due to limitations in system hardware and constraints in post-processing method, the minimum controllable layer thickness for printing is 50 μm. Consequently, the achievable range for controlled curing time spans from 0.5 s to 1 s, corresponding to a layer thickness range of 50 μm to 100 μm (step size: 10 μm).

PLLP achieves printing through projecting elongated lines. The projection within a range of 200 μm from the printing window has a resolution of 50 μm (figure S2), which also determines the minimum voxel length in the Z direction. In order to achieve a precise approximation for tubular structures, it is necessary to narrow down the projection as much as possible in the θ direction. To achieve this, we guide the projection through a fixed-width slit to modify its width, which is affixed to the printing window. Therefore, the width of the slit dictates the precision in the θ direction. After the slit narrows, the projection induces free radicals within the resin to initiate curing in the printing window. Despite the micron-scale width of the slit, the solidification thickness γ is within a similar range, rendering it insufficient to trigger diffraction. Thus, within the γ range, the optical field of the projection remains unaltered, preventing diffraction. However, as the width of the slit approaches the wavelength λ, the number

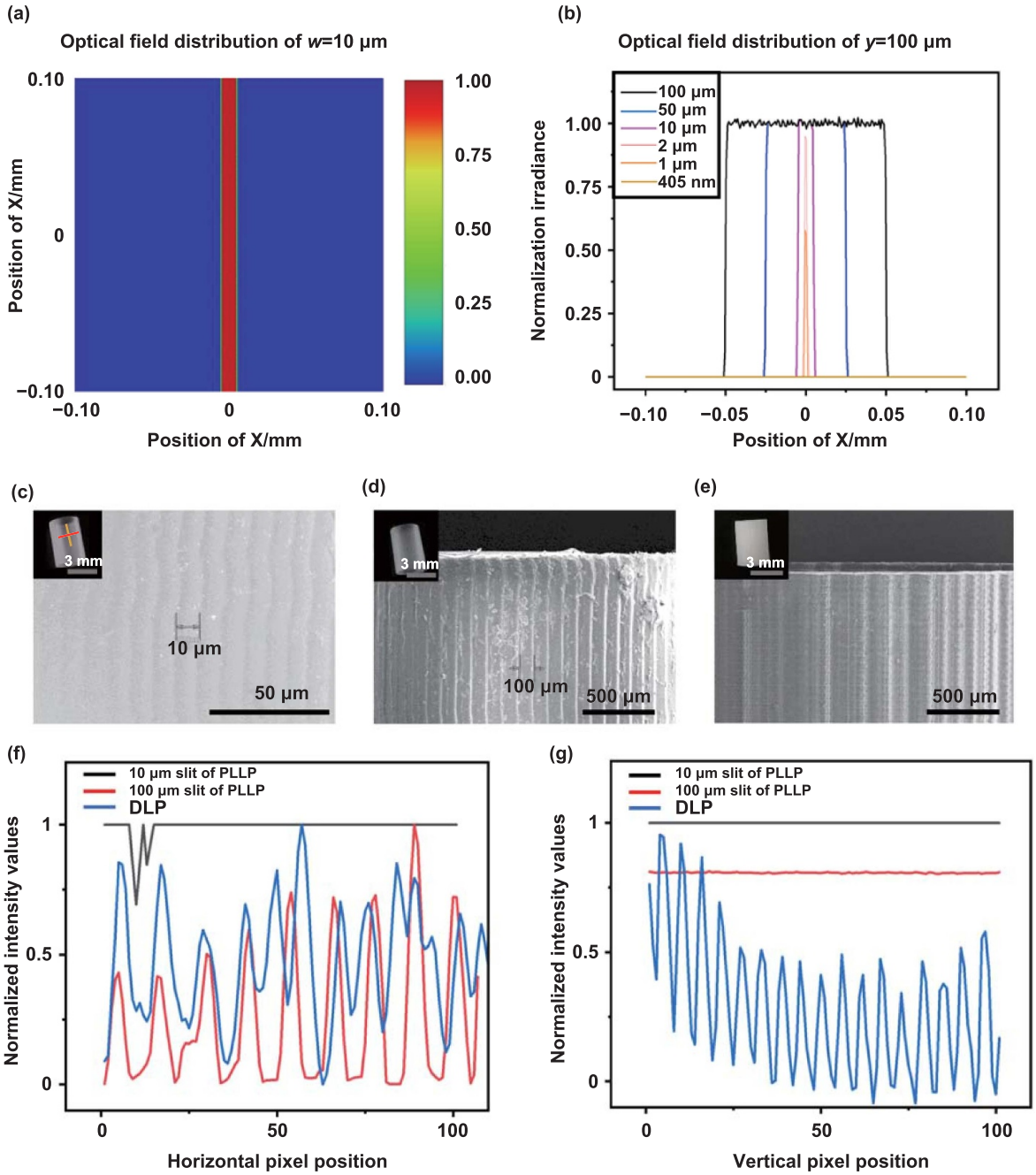

Figure 2. The slits resolution of PLLP. (a) and (b) Depict the light field distribution after the projection passes through the slits, simulated using Zemax. (a) Normalization irradiance of optical field distribution at a distance of $\gamma = 100$ μm from a $w = 10$ μm slit. (b) Normalization irradiance of X cross-sectional for the optical field distribution at a distance of $\gamma = 100$ μm from slits of varying widths. (c) and (d) are the tube structures of $r = 1.5$ mm, $\gamma = 50$ μm and $h = 8$ mm with $w = 10$ μm and $w = 100$ μm printed by PLLP, respectively. (e) The tube structure fabricated through DLP printing with parameters $r = 1.5$ mm, $\gamma = 200$ μm, and $h = 8$ mm. (f) and (g) correspond to the pixel-normalized values of the tube structure at the positions indicated by the red horizontal line and the yellow vertical line in (c), respectively, under electron microscopy with conditions set at 5.0 kV $\times$ 30 LM (UL). The black line represents PLLP with a width of $w = 10$ μm, the red line represents PLLP with a width of $w = 100$ μm, and the blue line represents the printing results from commercial DLP.

of photons passes through the slit diminishes, causing the projection to hardly pass through the slit (figures 2(a) and (b)). Ultimately, we employed femtosecond laser cutting to create metal sheets with slits of both 10 μm, 50 μm and 100 μm in width, with 10 μm being the smallest width feasible for our fabrication process. Utilizing these slits of widths $w = 10$ μm and $w = 100$ μm, we successfully printed tubes with a 3 mm inner diameter. Microscopic images reveal that the smallest features in the θ direction of the printed object are consistent with the width of the slit (figures 2(c) and (d)). Thus, by manipulating the slit width, we achieved printing precision of at least 10 μm in the θ direction.

Due to the difficulty in achieving the formation of tubular structures with wall thickness below 200 μm using DLP technology, we employed commercial DLP printing to produce tubes with the same height and inner diameter but a wall thickness of $\gamma = 200$ μm for surface smoothness comparison. It can be observed that the surface of tubes printed with commercial DLP exhibits pronounced layering (figure 2(e)). Under the same electron microscopy magnification (5.0 kV $\times$ 30 LM (UL)), we selected pixel grayscale values from the yellow vertical line and red horizontal line sections of the tube structure in figure 2(c), and compared them with the corresponding positions in figures 2(d) and (e), as shown in figures 2(f) and (g) (SEM images in figure S3). Within the red line region, the print structure of PLLP with a width of $w = 10$ μm is remarkably smooth, with the curve showing minimal variation. Conversely, both commercial DLP and the print structure with $w = 100$ μm exhibit protrusions that affect surface smoothness. The curve for commercial DLP shows more fluctuations. Similarly, within the yellow line region, the print structure of PLLP with a width of $w = 10$ μm is very smooth, with no apparent variation in the curve. In contrast, the commercial DLP print structure displays multiple fluctuations, and the curve for PLLP with $w = 100$ μm shows minimal undulation. This indicates that PLLP is more conducive to the manufacturing of tubular structures with smoother surfaces.

2.2. Slicing algorithm

Compared to conventional printing techniques which are based on the Cartesian coordinate system, i.e. *x, y, z* coordinate system, the PLLP technique needs a different slicing algorithm to print the vascular structure, which should be developed based on the polar coordinate system. The vascular 3D object would be sliced along the radial direction of the tube, and each layer is in a circle shape, which is greatly challenging to integrate with a printer. Inspired by the cyclotomic method, we develop a slicing algorithm PLS for the 3D structures. The closest shape to a circle is a square polygon centered at the center of the circle, and the more sides the closer to the circle. As shown in figure 1(b), a three-dimensional polar coordinate system is established with the intersection point between the center of the print mandrel and the highest part of the projection as the origin O. Once the printing layer thickness is established, the model is segmented into L layers by incrementing γ through the mandrel radius as the minimum radius. Finally, the three-dimensional model is sliced, starting from the point of intersection between the mandrel and the slit. Each layer is sliced into p_j segments based on the width of the slit. Initially, calculate the polar angle θ_j corresponding to the slit for the jth layer:

$$\theta_j = 2\arcsin\frac{w}{2(\gamma j + r)}, j = 1, 2, \ldots, L \tag{1}$$

where r is the print mandrel radius. L is the total number of layers of the print model and γ is the layer thickness. According to θ, the number of projections of the jth layer p_j, can be calculated:

$$p_j = \lceil 2\pi / \theta_j \rceil, j = 1, 2, \ldots, L \tag{2}$$

where $\lceil\rceil$ is rounded upward to ensure that the projection of the j layer is completely closed. PLS algorithm decomposes the 3D model into print projection based on p_j. After completing the model slicing, each projection is arranged in the same direction (either counterclockwise or clockwise), and the projections in each layer are arranged from the innermost layer near the mandrel outward. To facilitate better coverage over the slit, the width of each projection is expanded significantly beyond the width of the slit, resulting in the generation of the final projection slices.

3. Printed vascular structures

3.1. Mechanical properties

In comparison to the vascular structure printed in the Cartesian coordinate system, the PLLP printing system offers great advantages in the enhanced mechanical properties of the vascular structure. As illustrated in figures 3(a) and (c), when printing relatively thin tubular structures (where the tube wall is only a few printing resolution widths), PLLP approximates the cylindrical model into a regular polygonal tube with side length equal to the width of the slit. In contrast to the layered stacking of square pixels forming the circular tube walls in commercial DLP, the radial forces in the regular polygonal tube of PLLP are more evenly distributed across the sections. This aids in mitigating stress concentration, reducing local stresses, and enhancing compressive strength. In commercial DLP-printed tubes, the stacked voxel blocks create a stepped structure (figures 3(b) and (d)), which may result in stress concentration, causing certain portions of the cross-section to bear larger stresses and consequently reducing its load-bearing capacity.

To validate the compressive strength of both printing methods, we create a tube sample with a 200 μm wall thickness and 6 mm inner diameter using each method's respective slicing approach. In the PLLP method, we approximated the tube with a regular polygonal structure based on the slit width of 100 μm. In commercial DLP, the slicing was done with a plane precision in the XY direction of 50 μm. Based on the different surface topology, we build two numerical model, one with the smooth surface to represent PLLP, another one is created based on the slicing image from commercial DLP (detailed simulation details can be found in figure S15). Subsequently, pressure was applied along the R direction of the tube. As expected, the tube printed using the PLLP (with smooth surface) method exhibited more uniform stress distribution, while the commercial DLP tube (with the unsmoothed surface coming from the layer stacking) experienced higher stress concentration on its lateral side (figures 3(e) and (f)). Furthermore,

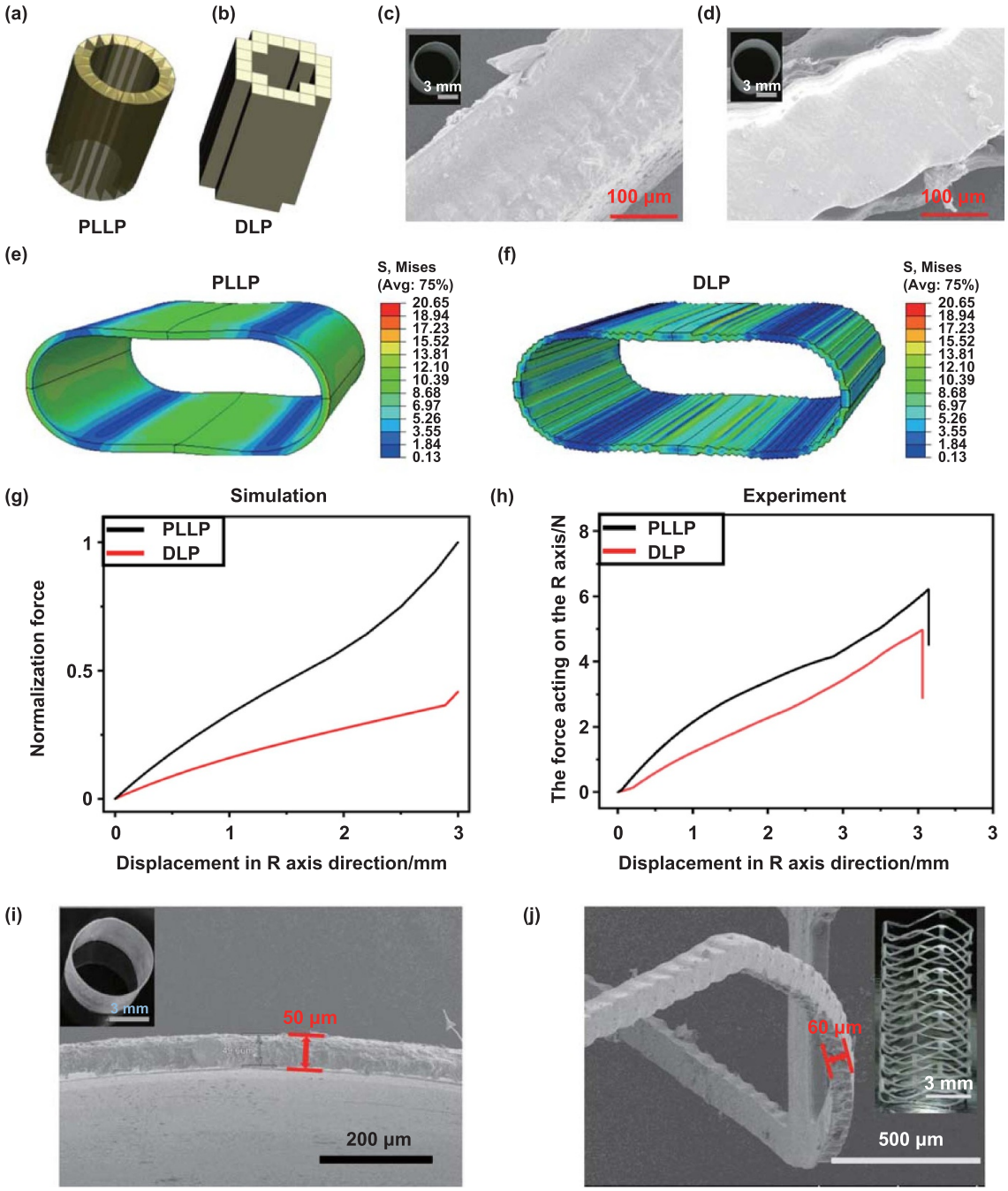

Figure 3. PLLP perfect circular printing compared to commercial DLP. (a) and (b) Diagram of a round tube printed using commercial DLP and PLLP, respectively. (c) and (d) Printing results of PLLP and commercial DLP of tube (model with wall thickness of $\gamma = 200$ μm, inner diameter of $r = 3$ mm, height of 6 mm). (e) and (f) Simulation of stress distribution schematic of the structure at 3 mm displacement printed by PLLP and commercial DLP, respectively. (g) Simulation of mechanical compression forces in the R direction for commercial DLP and PLLP. (h) Mechanical compression force measurements in the R direction for commercial DLP and PLLP. (i) Tube structure of $r = 3$ mm, $\gamma = 50$ μm, $h = 6$ mm with slit weight of $w = 100$ μm printed by PLLP. (j) Tubular graft of $r = 3$ mm, $\gamma = 60$ μm, $h = 12$ mm with slit of $w = 50$ μm printed by PLLP.

normalized stress curves indicated that, for the same compression distance, the tube printed with PLLP method could bear higher stress compared to the commercial DLP-printed tube. The strength with the PLLP method is approximately twice that of tube printed with the commercial DLP (figure 3(g)). Similarly, under conditions identical to the simulated slicing, we printed the tubular structures using both methods (figures 3(c) and (d)) and tested their stress using a compression machine. With a consistent compression speed of 3 mm min^{-1}, the stress curves obtained (figure 3(h)) clearly demonstrate that the stress from PLLP printing significantly surpasses that from commercial DLP. The strength with the PLLP method is approximately 1.4 times that of tube printed with the commercial DLP-printed. However, it is worth noting

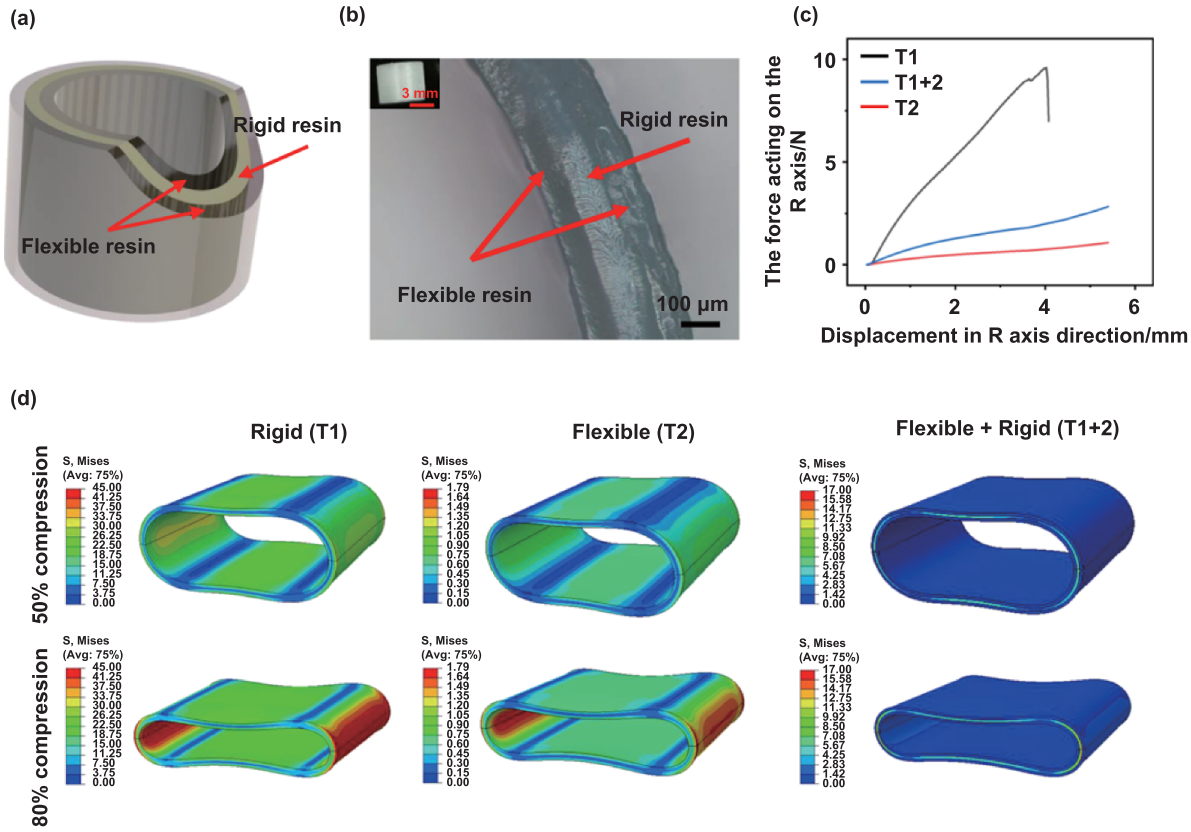

Figure 4. The pressure testing of the multi-material sandwich tube structure. (a) 3D model of the sandwich tube. (b) PLLP printing results and optical microscope images of the sandwich tube. (c) Radial pressure testing curves for the sandwich tube T1 + 2, rigid resin tube T1, and flexible resin tube T2. (d) Simulation plots of radial stress for the three tube types.

that in practical printing, commercial DLP-printed tubes have excess curing at the edges, which can increase the strength of tube. Consequently, simulated test results may underestimate the actual strength. Moreover, due to the inability to introduce support structures for thin-walled tubes, commercial DLP struggles to print tubular graft structures with thin walls and dimensions much larger than the wall thickness, especially when the wall thickness is just a single pixel's precision (figure S4). In contrast, PLLP, benefiting from its mandrel as a support, can print tubes with extremely thin walls, with a minimum wall thickness achievable down to 50 μm (figure 3(i)). Furthermore, the thin-walled tubular graft structures printed using PLLP maintain excellent flexibility, recovering their original shape after compression, stretching, and bending in various directions. As depicted in figure 3(j), a tubular graft structure with a 60 μm wall thickness remains intact even after being compressed, stretched, and bent to the maximum extent, eventually returning to its original form (movie 2–movie 4).

In addition, PLLP can print multi-material structures in the radial direction, combining the advantageous characteristics of two materials for complementary benefits. As shown in figure 4(a), a tube model T1 + 2 with a sandwich structure is presented, where both the inner and outer sides of the tube are printed using flexible resin, and the middle layer employs rigid resin, with equal thickness for all three layers. The flexible resin exhibits a high fracture elongation (132%) but a small elastic modulus (1.3 MPa), while the rigid resin has a high elastic modulus (527 MPa) but a low fracture elongation (20%). Due to both resins being acrylic resins, they adhere well between cured layers (figure 4(b)), and there are no visible gaps observed in the electron microscope image (figure S3(d)). To validate the superior performance of the multi-material tube, three tube structures were printed: T1, a tube printed with rigid resin. T2, a tube printed with flexible resin. The height and inner diameters of T1, T2, and T1 + 2 are all $h = 6$ mm and $r = 3$ mm, with a thickness of $\gamma = 300$ μm. Pressure tests were conducted on the three tubes, and the testing curves are shown in figure 4(c). It is observed that T1 fractures at a compression distance of 4 mm (67%), while T1 + 2 does not fracture even at full compression (90%), demonstrating superior compressive strength and resilience compared to individual materials. The slope of T1 + 2 is twice that of T2, indicating that by changing the thickness of the rigid resin layer by 100 μm, the compressive strength of the multi-layered tube is doubled, while compression level remains unchanged. As shown in figure 4(d), simulation compression experiments were conducted, simulating the radial force on the sandwich tube T1 + 2 and the rigid resin tube T1, and flexible resin tube T2. Under the action of a displacement load, both rigid and elastic resins exhibit consistent deformation and stress distribution. Significant deformations and stresses are observed at the left and right ends of the inner and outer layers, rendering them susceptible to failure and fracture. Despite similar deformation amplitudes, the rigid resin, boasting a higher elastic modulus, demonstrates superior

load-bearing capacity. For T1 + 2 resins, the deformation in the middle layer is comparatively smaller than that in T1 and T2 resins. In contrast, deformation predominantly occurs in the elastic resin regions of the inner and outer layers, effectively leveraging the deformation advantages of elastic resin and enhancing damage resistance compared to T1. However, stress in the middle layer of multi-material printing surpasses that in the inner and outer layers. Exploiting the high modulus of rigid resins in the middle layer enhances the load-bearing capacity of T1 + 2 compared to T2. In summary, T1 + 2 optimally harnesses the exceptional damage resistance of flexible resins and the robust load-bearing capacity of rigid resins. This synergistic approach enhances the overall toughness and stiffness performance of the material.

3.2. Printing speed

In contrast to CLIP, which maintains a dead zone beneath the advancing portion by introducing oxygen through the liquid resin below, and to HARP, which employs a movable liquid interface to reduce adhesion between the interface and the printed object for achieving continuous and rapid printing, PLLP achieves continuous and rapid printing through a simpler approach. During the printing process, as each projection is completed, the just-solidified portion is automatically detached from the projection window's position by the rotational mandrel. In this interval, resin replenishment occurs rapidly, taking only a few milliseconds. Since the distance between the mandrel and the window remains constant after rotation, there is no need to adjust the mandrel's position, the next projection can begin immediately. A crucial aspect of this process is ensuring that the cured resin adheres firmly to the auxiliary mandrel while being easily detachable from the reaction window's walls. To achieve this, optically clear polyperfluoroethylene propylene (FEP) silicone-adhesive tape (FEP transparent tape) was applied to the reaction window and the walls of the slot perpendicular to the projection, reducing the adhesion between the cured part and the reaction window's walls to below the adhesion with the mandrel (figure 5(a)) [42]. Resin with the same surface area was cured on both the axis and FEP. The force required to detach the cured portion from FEP was found to be significantly smaller than the force required for detachment from the mandrel (figure 5(b)).

Furthermore, the slicing approach of PLLP inherently leads to faster printing speeds for thin-walled, elongated tube structures, especially those that can be formed in a single layer. When a printing method can achieve continuous printing, the printing speed is solely determined by the number of projections and the exposure duration per projection. With a fixed exposure duration, determining the number of projections p allows us to deduce the printing time. The number of projections is closely related to the inner radius r and slit width w of the printed model, with the model's height having a minimal impact. Using formulas (1) and (2), we can calculate the variations of the polar angle θ and p for different r and w. As shown in figure 5(c), θ and p are inversely proportional, and with an increase in r, the number of projections p increases, implying longer projection times. Moreover, the slit width w also influences the number of projections, with the number of projections for a 10 μm slit being ten times that of a 100 μm slit when r is constant. PLLP exhibits exceptionally rapid forming speeds when printing structures with elevated heights, small inner diameters, and thin walls. At $w = 100$ μm, a single-layer tubular graft with $r = 1.5$ mm, $\gamma = 100$ μm and $z = 25$ mm height can be printed in less than 100 s (figure 5(d)). This is faster than 11.3 min of CLIP of 2 cm long, which is quite a big-bang when looking at the whole additive manufacturing technology. In addition to single-layer vascular structures, PLLP can be utilized for printing multi-layered structures such as screwdriver handles and enable wall-to-wall printing of tubes. In the multi-layer printing process of the screwdriver handle, as the number of layers increases, the corresponding θ of the slit decreases. The 12-layer structure with a layer thickness of $\gamma = 100$ μm and slit of $w = 100$ μm requires 1005 projections and the printing process takes 16 min (figure 5(e)). Figure 5(f) depicts the wall-adhered printing effect on the rotating mandrel, including Beihang University's emblem shape and some Chinese characters, using a slit width of $w = 10$ μm, mandrel of $r = 3$ mm and $r = 1.5$ mm, respectively. The lettering on the mandrel is distinctly visible. Similarly, employing a $w = 10$ μm slit, $\gamma = 50$ μm and a mandrel of $r = 1.5$ mm, we printed a more intricate tubular graft structure, yielding printed results nearly identical to the 3D model (figure 5(g)).

Compared to printing methods based on Cartesian coordinates, PLLP is suitable for printing thin tubular structures with a layer count z in the Z direction, greater than the number of projections p in the θ direction. As shown in figure 5(h), we compared the speed and resolution of several printing techniques for scaffold-like structures, including FDM [33, 43–46], CLIP [17, 31, 47], melt electrowriting [48], HARP [19], and CAL [23–25]. FDM has a low printing resolution, generally greater than 100 μm, and slow printing speed. HARP has faster print speeds, but the print resolution is low, greater than 100 μm compared to FDM. CAL has a very fast printing speed, but when the printing resolution reaches 20 μm, it can only print millimeter size due to the smaller projection [25]. CLIP produces relatively fast prints, but slows down due to the small projected size when printing at resolutions approaching 10 μm. CLIP has a resolution of single-digit microns. The printing resolution of PLLP is determined by the slit width w, ranging from a maximum of 100 μm to a minimum of 10 μm. Based on the relationship between p and z, the maximum volume of tubular structures printed by PLLP per minute under different slit widths can be calculated using formula S2. When $z = p$, the printing speed of PLLP falls within the range of FDM. However, the printing resolution is higher compared to the FDM method. When z is ten times p, the printing speed of PLLP is comparable to CLIP and CAL. When z is several tens of times p, PLLP's fastest printing speed far exceeds CLIP. When z is greater than 30 times p, PLLP is faster than CLIP at the same print resolution.

3.3. Multi-material printing

Using the Cartesian coordinate system-based photopolymerization printing method fails to achieve multi-material printing

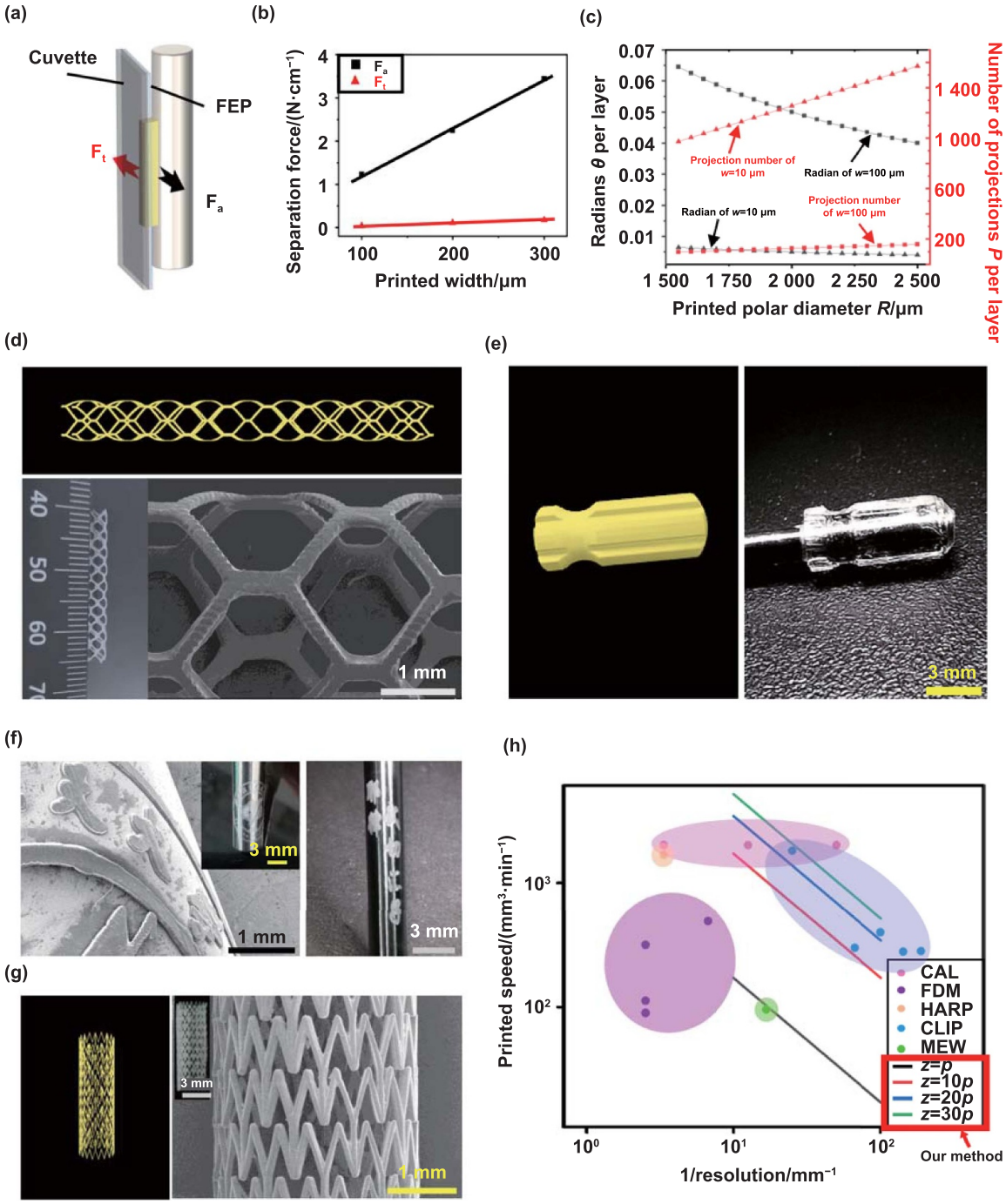

Figure 5. Demonstration attached prints from PLLP and print speed characterization. (a) Schematic diagram of the forces on the curing area. The adhesion force F_t of the cured part to the optically clear polyperfluoroethylene propylene (FEP) and F_a to the auxiliary rotary mandrel after the fine seam is projected. (b) Printing strips of widths of 100 μm, 200 μm, and 300 μm under slit width of $w = 100$ μm and height of 10 mm, respectively, on both FEP and the mandrel. The change of the values of F_t and F_a after curing different widths. (c) Variation of printing radii, projection count, and corresponding polar angles with different slit widths. (d), (e) and (g) are the 3D models of prints: high single layer tubular graft of 2.5 cm high, screwdriver handle. And, the yellow color represents the 3D models. (f) Wall-attached patterns on the mandrel and thin single layer tubular graft printed by slit of $w = 10$ μm, mandrel of $r = 3$ mm and $r = 1.5$ mm, respectively. (h) Comparison plot of print speed and resolution between PLLP and other 3D printing technologies. The lines of $z = p$, $z = 10p$, $z = 20p$, and $z = 30p$ represent our method.

with specified polar radii layers in vascular structures, whereas the FDM approach suffers from low printing accuracy in multi-material printing. However, PLLP, with the auxiliary of a rotating mandrel, allows for seamless material switching during printing without compromising the integrity of the already printed structures, all accomplished within a mere 10 s.

This method enables both single-layer multi-material printing and multi-layer multi-material printing (figures 6(a)–(d)).

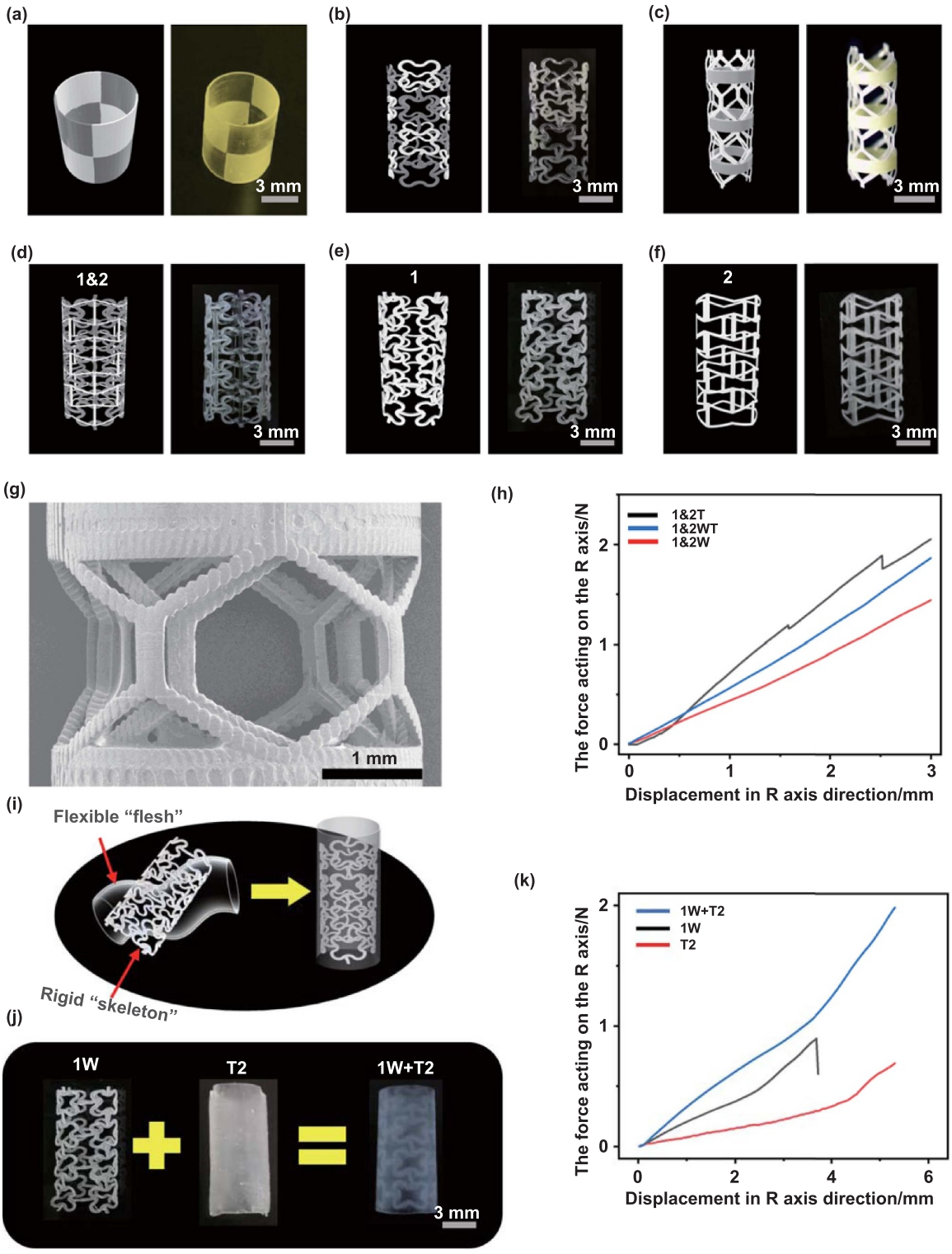

Figure 6. Demonstration of multi-material prints from PLLP. (a)–(f) represent the design models and the final printed structures, where the left side shows the 3D models and the right side depicts the printed structures. (a) The double material tube. (b) The double material tubular graft. (c) Three-layer tubular graft structure. The 1st and 3rd layer are white resins and the 2nd layer is yellow resin. (d) Composite tubular graft structure. (e) Structure 1 and (f) structure 2 can be printed by different resins. (g) 30x electron microscope picture of (c). (h) Mechanical compression force measurements in the *R* direction for composite tubular graft structures. (i) Schematic representation of the 'flesh + skeleton' configuration. (j) Rigid scaffold structure 1W, flexible tubular structure T2, and their combined structure 1W + T2. (k) Compression testing curves in the *R* direction for structures 1W, T2, and 1W + T2. Photographic documentation of the three structures during compression and post-recovery in figure S5.

Figure 6(a) depicts a single-layer tubular structure printed using two different-colored resins. In the printing process, the white resin part is initially printed, followed by resin replacement using a pump to complete the yellow resin part. Similarly, the printing of single-layer tubular graft structures with multiple materials can be achieved (figure 6(b)). Figure 6(c) is composed of three layers, where the first and third layers are connected by three annular structures in the middle layer, with the remaining parts disconnected apart from the annular sections. This three-layer structure necessitates two resin changes to complete the printing process. Figure 6(g), an electron microscope image, clearly depicts the central void in this structure.

Multi-material printing has certain advantages for tubular grafts. For biodegradable tubular grafts, it is not only necessary to have a precise manufacturing process but also ensure that the tubular graft's mechanical properties comply with medical requirements. This means that the tubular graft should not only be flexible enough for easy implantation but also possess sufficient radial rigidity to support the blood vessel. Achieving these dual requirements necessitates the use of various materials with different mechanical properties to create composite tubular grafts [49]. PLLP method is well-suited for such structures, we printed tubular graft structures using combinations of two resin materials with different elastic modulus. Among these, structures 1 and 2 exhibit varying radial stresses. Combining the two structures yields a stronger compressive resistance in structure 1&2. The elastic modulus of the white resin is lower than that of the transparent resin. Consequently, the compressive strength of structure 1&2T printed with the transparent resin surpasses that of structure 1&2W printed with white resin. The compressive strength of structure 1&2WT, printed with a blend of the two resins, lies between these two (figures 6(d)–(f) and (h)). PLLP enables alternate printing of materials with different modulus, further enabling the tuning of mechanical properties. In this case, structures 1&2WT achieved a 20% change in strength relative to 1&2W and a 10% change in strength relative to 1&2T (figure 6(h)).

Furthermore, the combination of soft and hard materials results in a more compressible and resilient structure, akin to the combination of 'flesh + skeleton' (figure 6(i)). PLLP enables the 3D printing of tubular models with a skeletal structure using both elastic and rigid resins, achieving high elasticity and strength. The tube section is printed with a flexible resin, while the embedded 'bone' section is printed with a rigid resin, with an inner radius of $r = 3$ mm and a height of $h = 12$ mm. Both the flexible and rigid resins are utilized in the sandwich tube structure of figure 4(b). Radial compression tests were conducted on individual 'flesh' structure T2 (layer thickness of $\gamma = 300$ μm), 'skeleton' structure 1W ($\gamma = 100$ μm), and the combined 'flesh + skeleton' structure 1W + T2 ($\gamma = 300$ μm) (figure 6(j)). It was observed that 1W + T2 and T2 did not fracture after compressing 5.4 mm, while the compressive strength of T2 was significantly lower than that of 1W + T2 and 1W (figure 6(k)). Structure 1W fractured at a compression distance of 3.7 mm. 1W + T2 maintained both high strength and resilience, exhibiting a 28% increase in resilience compared to 1W and a 2.8-fold increase in compressive strength compared to T2. This radial multi-material structure holds promising applications in areas such as artificial blood vessels and aerospace. Similarly, we printed tube structures with different materials to validate the multi-material printing capability of PLLP (figure S6).

PLLP technology is advantageous for radial multi-material tubular structure and long thin tubular structure printing, but for other types of model printing, is more time-consuming. The printing resolution of PLLP is determined by the width of the slit, and it can achieve the centimeter size model printing. CAL, CLIP and HARP can achieve the fast printing of arbitrary models, but the high resolution CAL has only millimeter size printing volume. For CLIP, high print speed and print resolution are available, but printing of multi-material structures is not achievable. The print speed of HARP is high but the print resolution is low, and the same as CLIP, it is not possible to print multi-material structures. FDM enables printing of multi-material structures, but the print resolution of FDM is low and the print speed is too slow. PLLP combines the characteristics of rapid printing through photopolymerization and the features of auxiliary axes to match tubular structures. To sum up, PLLP technology enables fast and high resolution printing of radial multi-material tubular structures as well as long thin tubular structures.

4. Conclusion

In this work, we present a novel continuous printing technology called PLLP, which relies on line projection. The rotational printing characteristic of PLLP automatically displaces the cured part away from the UV-transparent window by the rotating mandrel following each curing process, thereby facilitating automatic continuous printing. This eliminates the need for complex technical instruments to achieve continuous printing, and avoids creating an area which cannot be cured above the UV-transparent window. In the system of PLLP, the support of the rotary mandrel enables the printing of tubes with a single-resolution wall thickness. We successfully printed tubes with a diameter of 6 mm, a wall thickness of 50 μm, and a height of 6 mm. And the θ direction of the polar coordinates can attain a resolution of up to 10 μm. Furthermore, PLLP facilitates the seamless replacement printing of different materials. Given the fixed rotary mandrel, the cured part can be molded without the need for additional support. By incorporating material switching and judging the design material of each layer, we have successfully realized material change printing. This novel method enables the combined printing of different functional materials. Remarkably, a tubular graft with a height of 2.5 cm and an inner radius of $r = 1.5$ mm can be printed in just 100 s. This substantial reduction in printing time makes it feasible to create custom tubular grafts in a mere 20 min, potentially revolutionizing tubular graft manufacturing. Furthermore, the printing material for the PLLP is not limited by viscosity, allowing it to be applied to a wider range of printing environments. Moreover, with the increase in illumination power (instead of 16.4 mW cm^{-2} currently), faster

forming speeds can be achieved, theoretically ensuring that the solidified portions remain attached to the rotary mandrel during rotation at maximum speed. These advantages make PLLP potentially capable of reducing the time and cost associated with the manufacturing of some biodegradable tubular grafts, dental products, and aerospace applications.

5. Materials and methods

5.1. Resin material

The resin used in the experiments is a commercial photocurable resin with three colors and three types (Transparent rigid resin: Voxelab 405 nm Photopolymer Resin, Voxelab, China. Transparent flexible resin: Dajian Flexible 600/-9/-8405 nm Photopolymer Resin, Dajian, China. White rigid resin and yellow rigid resin: *e*sun standard resin, *e*sun, China), the elastic modulus of these three types of resin is different (figure S7). All these resins belong to the class of acrylate-based oligomers.

5.2. PLLP hardware design

PLLP high-speed tubular 3D printing system consists of 3 parts of hardware, (i) projection component using a DLP (DLP4710UV, TEXAS INSTRUMENTS, America) with 405 nm light source and projection accuracy of 45 μm–55 μm. Optical slits are added to the projection on the way to make the projected shape linear. Optical slit using a femtosecond laser (FCPA-uJewel D-1000, IMRA, America) to process a 0.05 mm thickness molybdenum sheet (figure S8). The resin tank is a customized high-transmittance cuvette with two liquid change ports at the bottom and optically clear FEP silicone-adhesive tape (FEP transparent tape, Taizhou Chenguang Plastic Industry Co., China) on the inner wall of the light-transmitting surface, with a light-transmitting slit fixed on the outer wall, which makes the adhesion of the cured part to the supporting shaft much stronger than to the projection wall. (ii) The liquid change ports are connected to the barrel that holds the resin used for printing through a tube, and the liquid change is controlled using Arduino Uno Rev3. motion control platform. (iii) The motion guides are assembled using linear slides (4080 U aluminum profile slides, sanweicube, China), with three slides that can be controlled individually, Z, R and θ. Each slide is controlled by a stepper motor to move (57HB56AL4, TimesBrilliant, China), and each motor is equipped with a separate drive module (DM542, Leadshine China). One of the rotating auxiliary axes (chrome-plated stainless steel bar, RuiFeng, China) is connected to the θ-axis motor by a high-precision collet (UP ER11, Fepri, China), and the collet and auxiliary axes are interchangeable. The printing process is controlled jointly by Raspberry Pi system (Raspberry Pi 4B, Raspberry Pi Foundation, UK).

5.3. Narrow slit diffraction simulation

Utilizing OpticStudio 18.9, simulate the diffraction pattern of a narrow slit. Configure the light source as a parallel rectangular source with a wavelength of 405 nm and a weight of 1.0. The slit is positioned at a distance of 2 mm from the light source. Set the receiving plane at a distance of 100 μm from the slit to observe the optical field distribution. In the simulation, consider only the propagation of light in a vacuum.

5.4. Printing and post-processing

The PLLP printing model is completed by six main steps, and the model is printed through the cycle (figure S9). After printing, remove the shaft with the printed sample from the motion control system and secondary cleaning with 95% alcohol. Then put in water above 80° and disengage by different coefficients of thermal expansion between the print shaft and the sample material. In order to achieve complete curing of the printed object, it is necessary to expose the printed sample under a UV lamp for more than 5 min. This prolonged exposure ensures that the Raman peak of the C=C bonds in the printed material ceases to decrease and no longer reacts with oxygen, leading the printed sample to attain its maximum curing limit (figure S10).

5.5. Slicing software and PLLP print control

The PLS slicing program for 3D models is programmed using python 3.9. First, the 3D file in STL format is read, calculate the number of projections using formulas (1) and (2), and sequentially label the slice positions. Then, store each sliced segment, with only 0 (no UV-light transmission) and 255 (full UV-light transmission) stored in the vector. The vector is then expanded into a matrix with a projection width much larger than the slit width. All the matrices are stored as images in the order of projection.

Projection, resin change and motor movement are controlled using python 3.9 play the projection after turning the auxiliary mandrel, the projection exposure time is determined according to the resin curing parameters, then stop the exposure to turn the auxiliary mandrel and start the projection again.

5.6. Stress simulation and measurements

All the simulation analyses corresponding to figures 3 and 4 were conducted using the ABAQUS/STANDARD analysis module. For simulations in figure 3, different printing methods were compared, and only the geometric differences between commercial DLP 3D printed object and PLLP 3D printed object were considered, with all other conditions being consistent. The geometric models of both objects were illustrated in figures S15(c) and (d). Specifically, the PLLP 3D printed object was depicted as a smooth cylindrical tube, resulting from its slicing approach (see figure S15(a)). On the other hand, the commercial DLP 3D geometry model was constructed as a stepped structure based on the slicing image from CHITUBOX V1.9.5. (refer to figure S15(c)), featuring a 40 μm radius fillet on each edge.

Linear elasticity constitutive models and C3D8R mesh elements were employed in both cylindrical tube objects. The young's modulus of printed white rigid resin was calculated

to be 527 MPa (see figure S7(c)). The upper part of the cylindrical tube contacted a rigid plate, symmetric boundary conditions were applied to the tube, and a uniform downward displacement boundary condition was applied to the central reference point of the steel plate with a constant velocity of 1.5 mm s^{-1} to enhance simulation speed. Additionally, the reaction forces and displacements in the normal direction at that point were extracted, allowing for the simulation of the compressive behavior of the entire cylindrical tube. Due to challenges in obtaining accurate pure material property values for both structures without including the stacking layers, simulations were employed for a qualitative comparison between the two printed objects. Normalization force was utilized and defined as the ratio of the force applied to a structure to the maximum force observed in both structures.

For figure 4, simulation analyses were conducted to qualitatively compare stress and strain distribution in different multi-material systems. The simulation settings for material constitutive models, mesh, and contact were kept consistent with those used in figure 3. The Young's modulus of white rigid resin and flexible resin were set to 527 MPa and 1.3 MPa, respectively, as calculated according to figure S7(c).

All stress experiments in this work were done under Shimadzu instruments. The pressure test in the *R* axis direction of the molded structure is carried out, and the force curve is obtained by compression at a speed of 3 mm min^{-1}.

5.7. Scanning electron microscopy

Scanning electron microscopy was used to obtain morphological images of the printed samples by secondary electron detection. The electron beam energy was 5 keV and the magnification ranged from 30x to 1000x. Gold plating was performed using a gold spraying instrument prior to the measurement.

Data availability statement

Data underlying this paper are available upon reasonable request.

Acknowledgments

This work was supported financially by the Fundamental Research Funds for the Central Universities (YWF-22-K-101, YWF-23-L-805 and YWF-23-YG-QB-006). We gratefully acknowledge the support from the National Natural Science Foundation of China (12372106) and Fundamental Research Funds for the Central Universities. The authors would also like to express our gratitude to Beijing Advanced Innovation Center for Biomedical Engineering.

Conflict of interest

Jiebo Li, Jianmin Han, Zhijian Wang, Xin Yan, Yubo Fan, Jiping Yang, Jingyong Sun, Huiyuan Wang, Xincheng Yin and Siqin Liu are inventors on the patents related to this work filed by Beihang University (No. CN115847806A, application on 29 November 2022). The authors declare that they have no other competing interests.

Contributions

Jiebo Li, Zhijian Wang, Jianmin Han, Yubo Fan and Xin Yan conceptualized the technique. Huiyuan Wang wrote printer control software, performed prints, and data analysis. Huiyuan Wang and Xincheng Yin built the printer system. Siqin Liu simulated the force distribution. Mingming Huang took electron microscope photographs. Yanzhe Fu analysed the impact of slit width on projection. Xun Chen guided the theory of light curing. Chao Wang, Jingyong Sun, Jianmin Han, Jiping Yang, Lizhen Wang and Yubo Fan analysed the data and discussed the experiments. Jiebo Li wrote the manuscript with input from all authors.

ORCID iD

Jiebo Li https://orcid.org/0000-0002-2295-6666

References

[1] Wang P J, Sun Y Z, Shi X Q, Shen H X, Ning H H and Liu H T 2021 3D printing of tissue engineering scaffolds: a focus on vascular regeneration *Bio-des. Manuf.* **4** 344–78
[2] Paunović N *et al* 2021 Digital light 3D printing of customized bioresorbable airway stents with elastomeric properties *Sci. Adv.* **7** eabe9499
[3] Park H S *et al* 2018 A 4-axis technique for three-dimensional printing of an artificial trachea *Tissue Eng. Regen. Med.* **15** 415–25
[4] Liang W, Das A, Dong X and Cui Z 2018 Lithium doped tubular structure in LiB_{20} and LiB_{20}^{-}: a viable global minimum *Phys. Chem. Chem. Phys.* **20** 16202–8
[5] Shen Z, Chen Y, Wang W and Zhao X 2010 Tubular structures in China: state of the art and applications *Proc. Inst. Civ. Eng. Struct. Build.* **163** 417–26
[6] Langi E, Zhao L G, Jamshidi P, Attallah M M, Silberschmidt V V, Willcock H and Vogt F 2021 Microstructural and mechanical characterization of thin-walled tube manufactured with selective laser melting for stent application *J. Mater. Eng. Perform.* **30** 696–710
[7] Guerra A J, Farjas J and Ciurana J 2017 Fibre laser cutting of polycaprolactone sheet for stents manufacturing: a feasibility study *Opt. Laser Technol.* **95** 113–23
[8] Meng H Y, Liao J H, Zhou Y H and Zhang Q M 2009 Laser micro-processing of cardiovascular stent with fiber laser cutting system *Opt. Laser Technol.* **41** 300–2
[9] Jia W T *et al* 2016 Direct 3D bioprinting of perfusable vascular constructs using a blend bioink *Biomaterials* **106** 58–68
[10] Grigoryan B *et al* 2019 Multivascular networks and functional intravascular topologies within biocompatible hydrogels *Science* **364** 458–64
[11] Popescu D, Zapciu A, Amza C, Baciu F and Marinescu R 2018 FDM process parameters influence over the mechanical properties of polymer specimens: a review *Polym. Test* **69** 157–66
[12] Layani M, Wang X F and Magdassi S 2018 Novel materials for 3D printing by photopolymerization *Adv. Mater.* **30** 1706344
[13] Ngo T D, Kashani A, Imbalzano G, Nguyen K T Q and Hui D 2018 Additive manufacturing (3D printing): a review of

materials, methods, applications and challenges *Composites* B **143** 172–96
[14] Dolinski N D *et al* 2021 Tough multimaterial interfaces through wavelength-selective 3D printing *ACS Appl. Mater. Interfaces* **13** 22065–72
[15] Macdonald N P, Cabot J M, Smejkal P, Guijt R M, Paull B and Breadmore M C 2017 Comparing microfluidic performance of three-dimensional (3D) printing platforms *Anal. Chem.* **89** 3858–66
[16] Park S A, Lee S J, Lim K S, Bae I H, Lee J H, Kim W D, Jeong M H and Park J K 2015 *In vivo* evaluation and characterization of a bio-absorbable drug-coated stent fabricated using a 3D-printing system *Mater. Lett.* **141** 355–8
[17] Tumbleston J R *et al* 2015 Continuous liquid interface production of 3D objects *Science* **347** 1349–52
[18] Hsiao K *et al* 2022 Single-digit-micrometer-resolution continuous liquid interface production *Sci. Adv.* **8** eabq2846
[19] Walker D A, Hedrick J L and Mirkin C A 2019 Rapid, large-volume, thermally controlled 3D printing using a mobile liquid interface *Science* **366** 360–4
[20] de Beer M P, van der Laan H L, Cole M A, Whelan R J, Burns M A and Scott T F 2019 Rapid, continuous additive manufacturing by volumetric polymerization inhibition patterning *Sci. Adv.* **5** eaau8723
[21] Regehly M, Garmshausen Y, Reuter M, König N F, Israel E, Kelly D P, Chou C Y, Koch K, Asfari B and Hecht S 2020 Xolography for linear volumetric 3D printing *Nature* **588** 620–4
[22] Hahn V, Rietz P, Hermann F, Müller P, Barner-Kowollik C, Schlöder T, Wenzel W, Blasco E and Wegener M 2022 Light-sheet 3D microprinting via two-colour two-step absorption *Nat. Photon.* **16** 784–91
[23] Kelly B E, Bhattacharya I, Heidari H, Shusteff M, Spadaccini C M and Taylor H K 2019 Volumetric additive manufacturing via tomographic reconstruction *Science* **363** 1075–9
[24] Loterie D, Delrot P and Moser C 2020 High-resolution tomographic volumetric additive manufacturing *Nat. Commun.* **11** 852
[25] Toombs J T, Luitz M, Cook C C, Jenne S, Li C C, Rapp B E, Kotz-Helmer F and Taylor H K 2022 Volumetric additive manufacturing of silica glass with microscale computed axial lithography *Science* **376** 308–12
[26] Orth A *et al* 2023 Deconvolution volumetric additive manufacturing *Nat. Commun.* **14** 4412
[27] Jiang H, Ziegler H, Zhang Z N, Zhang H, Le Barbenchon L, Atre S and Chen Y Y 2022 3D printed tubular lattice metamaterials for mechanically robust stents *Composites* B **236** 109809
[28] Hua W J, Shi W L, Mitchell K, Raymond L, Coulter R, Zhao D Y and Jin Y F 2022 3D printing of biodegradable polymer vascular stents: a review *Chin. J. Mech. Eng. Addit. Manuf. Front.* **1** 100020
[29] He Q S, Zhao Z F, Zhang H, Duan J J, Zhang N, Cui K K, Zhong Q Y and Yang C L 2023 Bioinspired adhesive manufactured by projection microstereolithography 3D printing technology and its application *Adv. Mater. Interfaces* **10** 2202465
[30] Wang X G, Li Z H, Liu J Q, Wang C Y, Bai H T, Zhu X J, Wang H, Wang Z H, Liu H and Wang J C 2023 3D-printed PCL scaffolds with anatomy-inspired bionic stratified structures for the treatment of growth plate injuries *Mater. Today Biol.* **23** 100833
[31] van Lith R, Baker E, Ware H, Yang J, Farsheed A C, Sun C and Ameer G 2016 3D-printing strong high-resolution antioxidant bioresorbable vascular stents *Adv. Mater. Technol.* **1** 1600138
[32] Ware H O T, Farsheed A C, Akar B, Duan C W, Chen X F, Ameer G and Sun C 2018 High-speed on-demand 3D printed bioresorbable vascular scaffolds *Mater. Today Chem.* **7** 25–34
[33] Jia H, Gu S Y and Chang K 2018 3D printed self-expandable vascular stents from biodegradable shape memory polymer *Adv. Polym. Technol.* **37** 3222–8
[34] Lee S J *et al* 2019 Heparin coating on 3D printed poly (l-lactic acid) biodegradable cardiovascular stent via mild surface modification approach for coronary artery implantation *Chem. Eng. J.* **378** 122116
[35] Wang C J, Zhang L, Fang Y C and Sun W 2021 Design, characterization, and 3D printing of cardiovascular stents with zero Poisson's ratio in longitudinal deformation *Engineering* **7** 979–90
[36] Singh J, Pandey P M, Kaur T and Singh N 2021 A comparative analysis of solvent cast 3D printed carbonyl iron powder reinforced polycaprolactone polymeric stents for intravascular applications *J. Biomed. Mater. Res.* **109** 1344–59
[37] Domínguez-Robles J, Shen T J, Cornelius V A, Corduas F, Mancuso E, Donnelly R F, Margariti A, Lamprou D A and Larrañeta E 2021 Development of drug loaded cardiovascular prosthesis for thrombosis prevention using 3D printing *Mater. Sci. Eng.* C **129** 112375
[38] Hu J C, Jian Z A, Lu C X, Liu N, Yue T, Lan W X and Liu Y Y 2021 New method for preparing small-caliber artificial blood vessel with controllable microstructure on the inner wall based on additive material composite molding *Micromachines* **12** 1312
[39] Wang M, Li W L, Mille L S, Ching T, Luo Z Y, Tang G S, Garciamendez C E, Lesha A, Hashimoto M and Zhang Y S 2022 Digital light processing based bioprinting with composable gradients *Adv. Mater.* **34** 2107038
[40] Kuang X, Wu J T, Chen K J, Zhao Z, Ding Z, Hu F J Y, Fang D N and Qi H J 2019 Grayscale digital light processing 3D printing for highly functionally graded materials *Sci. Adv.* **5** eaav5790
[41] Chien H L and Lee Y C 2020 Three dimensional maskless ultraviolet exposure system based on digital light processing *Int. J. Precis. Eng. Manuf.* **21** 937–45
[42] Kowsari K, Akbari S, Wang D, Fang N X and Ge Q 2018 High-efficiency high-resolution multimaterial fabrication for digital light processing-based three-dimensional printing *3D Print. Addit. Manuf.* **5** 185–93
[43] Mazzanti V, Malagutti L and Mollica F 2019 FDM 3D printing of polymers containing natural fillers: a review of their mechanical properties *Polymers* **11** 1094
[44] Guerra A J and Ciurana J 2018 3D-printed bioabsorbable polycaprolactone stent: the effect of process parameters on its physical features *Mater. Des.* **137** 430–7
[45] Wu Z C, Zhao J, Wu W Z, Wang P P, Wang B F, Li G W and Zhang S 2018 Radial compressive property and the proof-of-concept study for realizing self-expansion of 3D printing polylactic acid vascular stents with negative Poisson's ratio structure *Materials* **11** 1357
[46] Zhao D Y, Zhou R Q, Sun J X, Li H X and Jin Y F 2019 Experimental study of polymeric stent fabrication using homemade 3D printing system *Polym. Eng. Sci.* **59** 1122–31
[47] Ware H O T, Farsheed A C, Baker E, Ameer G and Sun C 2017 Fabrication speed optimization for high-resolution 3D-printing of bioresorbable vascular scaffolds *Proc. CIRP* **65** 131–8
[48] Somszor K, Bas O, Karimi F, Shabab T, Saidy N T, O'Connor A J, Ellis A V, Hutmacher D and Heath D E 2020 Personalized, mechanically strong, and biodegradable coronary artery stents via melt electrowriting *ACS Macro Lett.* **9** 1732–9
[49] Guerra A J, Cano P, Rabionet M, Puig T and Ciurana J 2018 3D-printed PCL/PLA composite stents: towards a new solution to cardiovascular problems *Materials* **11** 1679